creative commons

COMMONS DEED

저작자표시-비영리-변경금지 2.0 대한민국

이용자는 아래의 조건을 따르는 경우에 한하여 자유롭게

- 이 저작물을 복제, 배포, 전송, 전시, 공연 및 방송할 수 있습니다.

다음과 같은 조건을 따라야 합니다:

저작자표시. 귀하는 원저작자를 표시하여야 합니다.

비영리. 귀하는 이 저작물을 영리 목적으로 이용할 수 없습니다.

변경금지. 귀하는 이 저작물을 개작, 변형 또는 가공할 수 없습니다.

- 귀하는, 이 저작물의 재이용이나 배포의 경우, 이 저작물에 적용된 이용허락조건을 명확하게 나타내어야 합니다.
- 저작권자로부터 별도의 허가를 받으면 이러한 조건들은 적용되지 않습니다.

저작권법에 따른 이용자의 권리는 위의 내용에 의하여 영향을 받지 않습니다.

이것은 이용허락규약(Legal Code)을 이해하기 쉽게 요약한 것입니다.

Disclaimer

dCollection

공학석사학위논문

레이놀즈수 60,000 에서 자동 디플렉터를 이용한 SD7003 익형의 실속 제어

Post-stall control on the SD7003 airfoil using an automatic moving deflector at Re=60,000

2016년 2월

서울대학교 대학원

기계항공공학부

천 소 민

레이놀즈수 60,000 에서 자동 디플렉터를 이용한 SD7003 익형의 실속 제어

Post-stall control on the SD7003 airfoil using an automatic moving deflector at Re=60,000

지도교수 최 해 천

이 논문을 공학석사 학위논문으로 제출함

2015년 10월

서울대학교 대학원

기계항공공학부

천 소 민

천소민의 공학석사 학위논문을 인준함

2015년 12월

위 원 장 김 호 영

부위원장 최 해 천

위 원 박 형 민

Post-stall control on the SD7003 airfoil using an automatic moving deflector at Re=60,000

Somin Cheon

Department of Mechanical & Aerospace Engineering

Seoul National University

Abstract

In the present study, we apply an automatic moving deflector (AMD), a bio-inspired control device from feathers of bird wings, to the suction surface of the SD7003 airfoil to investigate its aerodynamic performances. We conduct a large eddy simulation at Re = 60,000 based on the chord length and free stream velocity. The angle of attack is fixed at a post-stall angle of 12 degree. The parameters of AMD are its length and tilting angle with the chord line. The results of the base airfoil without AMD agree well with previous experimental data. The AMD significantly reduces the flow separation and subsequently the drag coefficient and force fluctuations.

Keywords: Large eddy simulation, SD7003 airfoil, Automatic moving deflector

Student number: 2012-23945

Contents

Abstract i

Contents ii

List of Figures iii

List of Tables v

Nomenclature vi

Chapter

1 Introduction 1

2 Numerical Details 4

2.1 Governing equations 4

2.2 Computational details 5

3 Numerical Results 9

3.1 Aerodynamic coefficients and flow structures for the SD7003 airfoil. 9

3.2 Aerodynamic coefficients for the controlled airfoils. 9

3.3 Comparing flow structures of the no controlled airfoil and the controlled airfoils. 10

3.4 Mean velocity and pressure profiles near the leading edge of the no controlled and the controlled airfoils. 11

3.5 Mean streamlines of the no controlled and the controlled airfoils.11

3.6 Comparison of the Mean surface coefficients for each cases ... 12

3.7 Instantaneous three dimensional vortical structures 12

4 Summary and Conclusion 27

Bibliography 28

List of Figures

FIGURE 2.1 Schematic diagram of the present LES. 7

FIGURE 2.2 Schematic diagram of the AMD's parameter (left) and Kim's experimental results (right). 8

FIGURE 3.1 The time traces of the drag (red solid line) and lift (blue solid line) coefficients of the no controlled SD7003 airfoil. 13

FIGURE 3.2 The instantaneous spanwise vorticity contour around the SD7003 airfoil. 15

FIGURE 3.3 Spanwise averaged pressure contour and three dimensional vortical structure around the SD7003 airfoil with the lift coefficient being local minimum. 16

FIGURE 3.4 Spanwise averaged pressure contour and three dimensional vortical structure around the SD7003 airfoil as the lift coefficient is local maximum. 17

FIGURE 3.5 The time traces of the drag and lift coefficients of the controlled airfoils (solid red lines) comparing with those of the no controlled airfoil (dashed black lines). 18

FIGURE 3.6 The instantaneous spanwise vorticity contours of the no controlled airfoil (left), the controlled case 1(middle) and the controlled case 3 (right). 19

FIGURE 3.7 The time traces of the lift and drag coefficients and spanwise averaged pressure contours of the no controlled case (dashed lines) and the controlled cases (red solid lines). 20

FIGURE 3.8 The time traces of the lift and drag coefficients and spanwise averaged pressure contours of the no controlled case (dashed line) and the controlled cases (solid red lines). 21

FIGURE 3.9 The velocity profiles near the leading edge of the controlled case 1 (red solid lines) and the no controlled airfoil (black solid lines). 22

FIGURE 3.10 The velocity and pressure profiles near the leading of the controlled case 1 and the no controlled airfoil. Solid and dashed lines indicate velocity and pressure profiles, respectively and black and blue lines indicates the no controlled and controlled cases, respectively. 23

FIGURE 3.11 The mean streamlines of the each cases. 24

Figure 3.12 The mean surface pressure coefficients of the no controlled case (red solid lines) and the each controlled cases (blue solid lines). 25

Figure 3.13 The instantaneous vortical structures around the airfoil with AMD using λ_2 −structures which are proposed by Jeong and Hussain for the no controlled case and the controlled case 2. .. 26

List of Tables

Table 3.1 The previous results of the numerical simulation for the SD7003 airfoil at the angle of attack, 12 degree. 14

Nomenclature

Roman Symbols

C_D	drag coefficient
C_L	lift coefficient
D	drag force
L	lift force
f_i	momentum forcing
p	pressure
q	mass source/sink
Re	Reynolds number
A	plan form area of airfoil
u_∞	free−stream velocity
d	location of the AMD
β	AMD's angle with chord length
c	chord length of airfoil
$\overline{C}$	mean exit streamwise velocity
u,v,w	streamwise, wall−normal and spanwise velocity components, respectively
x,y,z	Cartesian coordinate (streamwise, wall−normal, spanwise direction)

Greek Symbols

α	angle of attack
ν	kinematic viscosity
ρ	density

Superscripts

$\overline{()}$	mean quantity

Abbreviations

AMD	Automatic moving deflector

Chapter 1

Introduction

In recent years, an interest on small Unmanned Aerial Vehicles (UAV) able to perform a wide range of missions has been developed from the onset of newly created micro system technologies. Due to their size and low air speed, these vehicles typically operate at Re on the order of $10^4 - 10^5$ (Galbraith *et al.,* 2008). At these low region of Reynolds numbers, the flow is laminar over a significant part of the airfoil and cannot endure even small adverse pressure gradients. At the proper angles of attack, separation leads to the formation of a laminar separation bubble (LSB) which breakdowns into turbulence prior to reattachment. The LSB moves towards the leading edge as increasing angle of attack and becomes smaller in streamwise direction. But the stall angle is exceeded, reattachment is no longer possible and bubble bursting occurs. The onset and successive breakdown of the LSB at low Reynolds number is known to be detrimental to performance of UAVs (Galbraith *et al.,* 2008).

On the other hand, one of the promising areas for enhancing aerodynamic performances is the bio-mimetic approach in which solutions to engineering problems are obtained from some morphological features of living creatures in nature (Choi *et al.,* 2012).

One impressive bio-mimetic solution is the flow control device inspired by the secondary feathers of a bird s wing. This concept was developed by Liebe (1979) who observed the flight of a bird

and noticed that the secondary feathers on the wing suction surface pop up while it lands. Liebe (1979) concluded that flow separation starts to develop on a wing, reverse flow occurs inside the separation bubble, and secondary feathers pop up responding to the reverse flow. This feathers prevent further propagation of flow separation, leading to the delay of flow separation. Although he pointed it out as a high-lift device of a biological wing, there had been no successful applications of this idea until the study of Bechert *et al* (1997). They implemented a movable deflector, mimicking the secondary feathers of a bird s wing, on two-dimensional airfoils, and observed the deflector movement and its aerodynamic performance. They also experimented it to a real flight by applying movable deflectors and gained lift enhancement. There also have been a few numerical studies for this device (Schatz *et al.,* 2004, Meyer *et al.*, 2007). Another researchers extended this application to the other airfoil models and experimented its performance (Kernstine *et al.,* 2008; Schlüter, 2010; Wang and Schlüter, 2012). This device results in lift enhancement at high angles of attack by reducing the flow separation from the trailing edge to the suction peak region.

We believe that the concept of this impressive bio-inspired flow control device should be also utilized to the flow at a low Reynolds region where UAVs are employed and SD7003 airfoil has good aerodynamic performances. Therefore, in our study, we apply this bio-mimetic device, called AMD (automatic moving deflector; inspired by the dynamics of the secondary feathers of a bird' s wing and the name AMD has already been designated at Kim *et al.,* 2014) hereafter, to a two-dimensional airfoil model (SD7003) for the enhancement of aerodynamic lift and the reduction of the

aerodynamic drag at post-stall angle of attack, 12° and investigate the mechanism responsible for aerodynamic benefits using large eddy simulations (LES).

Chapter 2

Numerical Details

2.1 Governing equations

The filtered governing equations of unsteady incompressible viscous flow for large eddy simulation on the Cartesian coordinate system are

$$\frac{\partial \overline{u}_i}{\partial x_i} - q = 0 \tag{1}$$

$$\frac{\partial \overline{u}_i}{\partial t} + \frac{\partial \overline{u}_i \overline{u}_j}{\partial x_j} = -\frac{\partial \overline{p}}{\partial x_i} + \frac{1}{Re_c}\frac{\partial^2 \overline{u}_i}{\partial x_j \partial x_j} - \frac{\partial \tau_{ij}}{\partial x_j} + f_i \tag{2}$$

Where $(\overline{\bullet})$ indicates the filtering operation, x_i's are the Cartesian coordinates, u_i's are the corresponding velocity components, p is the pressure, f_i and q, respectively, are the momentum forcing and the mass source/sink defined on the immersed boundary or inside the body (Kim *et al.* 2001). Dynamic global model proposed by Park *et al.* 2006 and Lee *et al.* 2010 are used for obtaining the sub-grid scale stress tensor $\tau_{ij} = \overline{u_i u_j} - \overline{u}_i \overline{u}_j$. All the variables are non-dimensionalized by the chord length c and the free-stream velocity u_∞. The Reynolds number is defined as $\mathrm{Re}_C = u_\infty c/\nu$, where ν is the kinematic viscosity. A staggered grid system is employed in this study, and thus u_i and f_i are defined at the cell face, whereas p

and q are defined at the cell center. The time-integration method used to solve (1) and (2) is based on a fractional step method. Hence a pseudo-pressure is used to correct the velocity field and then the continuity equation is satisfied at each computational time step. In this study, we use a second-order linearized fully implicit time advancement scheme as in Kim *et al.* 2001. Also spatial discretization are handled with second-order central difference scheme.

2.2 Computational details

Figure 2.1 shows the schematic diagram of the computational domain and boundary conditions. As explained before, we use the Cartesian coordinate system, where x, y and z, respectively, denote the streamwise, wall-normal and spanwise directions. The computational domain size in free-stream condition is $-7.5 \le x/c \le 7.5$, $-7.5 \le y/c \le 7.5$ and $0 \le z/c \le 1$, where $x/c = 0, y/c = 0$ corresponds to the leading edge of the airfoil. The computational domain has periodic boundary condition along the spanwise direction in order to simulate an infinite wing. Non0uniform meshes are used with dense resolution in the vicinity of body to accurately capture the separation, transition and reattachment, as well as the average pressure coefficient profile along the airfoil surface. Consequently, after the considerable grid convergence test, the numbers of grid points are $769(x) \times 449(y) \times 161(z)$.

A Dirichlet boundary condition ($u = U_\infty, v = 0, w = 0$) is used at the inflow and bottom. Neumann boundary conditions are applied to the

normal and spanwise component ($\partial v/\partial y = 0, \partial w/\partial y = 0$) at top boundary. For the outflow boundary, a convective boundary condition ($\partial u_i/\partial t + \overline{C}\,\partial u_i/\partial x = 0$) is used, where $\overline{C}$ is the space-averaged streamwise velocity at the exit. AMDs' parameters are the locations (d=0.2c, 0.35c, *0.5c*) and the tilting angles ($\beta = 10^\circ, 7^\circ, 7^\circ$) of AMDs based on Kim's experiment (Figure 2.2). Angle of attack (α) is 12°.

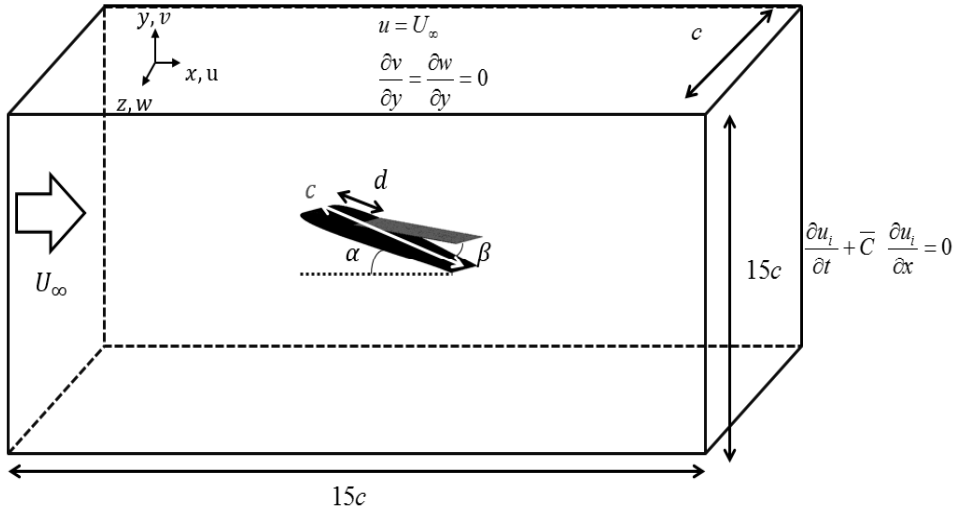

FIGURE 2.1 Schematic diagram of the present LES.

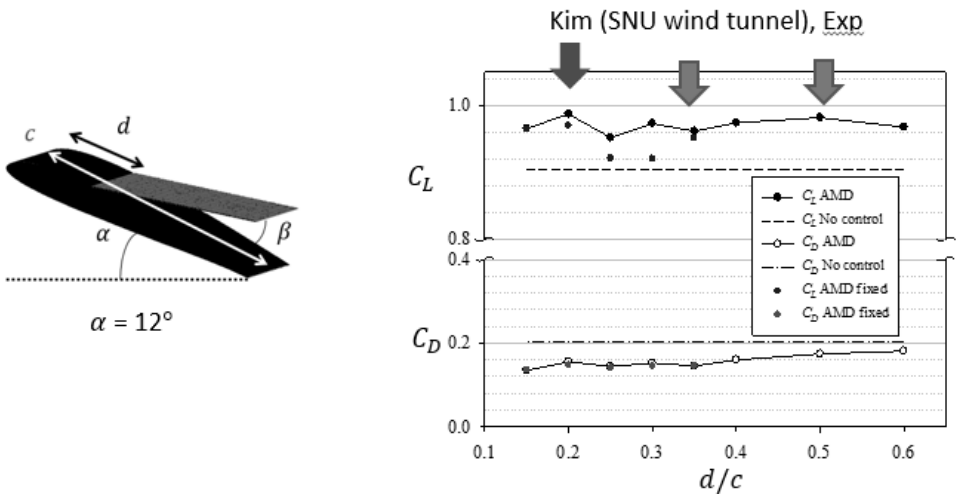

FIGURE 2.2 Schematic diagram of the AMD's parameter (left) and Kim's experimental results (right).

Chapter 3

Results and Discussions

3.1 Aerodynamic coefficients and flow structures for the SD7003 airfoil

In this chapter, we discuss the results of the no controlled base airfoil and controlled airfoils. Figure 3.1 and 3.2 are the results of the no controlled SD7003 airfoils. Fig 3.1 shows the time traces of drag and lift coefficients respectively. There has been several reports of aerodynamic coefficients for the SD7003 airfoil at post stall angle of attack. Table 3.1 shows the results of the previous studies. In the present study, mean lift and drag coefficients are 0.82 and 0.19 respectively and these values are generally agreed with the other data.

Figure 3.2 is the instantaneous spanwise vorticity contour around the SD7003 airfoil. As seen in this figure, the SD7003 airfoil has leading edge separation at this angle of attack and complex vortical structures at the suction side of the airfoil. Large separation bubble grows from the leading edge and develops to the downstream.

The lift coefficient is local minimum when developed leading edge separation bubbles burst at the suction side of the airfoil and the lift coefficient is local maximum when leading edge separation bubbles grow and develop to the downstream (Figure 3.3 and 3.4).

3.2 Aerodynamic coefficients for the controlled airfoils

Figure 3.5 is the time traces of each controlled cases compared

with the no controlled case. Black dashed lines are the lift and drag coefficients of the no controlled case respectively. Red solid lines are those of the controlled case respectively. All of the controlled cases are represents both lift enhancements and drag reductions. The force fluctuations of the case 1and 2 are reduced by AMDs but the force fluctuations of the case 3 are similar with those of the no controlled airfoil.

Case 1 and 2 shows similar force traces, so case 1 and 3 are selected for explaining the flow structures and comparing with the no controlled case.

3.3 Comparing flow structures of the no controlled airfoil and the controlled airfoils

Figure 3.6 is the instantaneous spanwise vorticity contours of each cases respectively. As shown this figure, a large leading edge separation bubble is reduced by AMDs and complex vortical structures are suppressed at the trailing edge.

Figure 3.7 and 3.8 show the time traces of the lift and drag coefficients and spanwise averaged pressure contour of the case 3 and 1 comparing with the no controlled airfoil respectively. The lift coefficient is local maximum when leading edge separation bubbles grow and develop to the downstream as shown in this figure. As comparing with the case 3 and 1, the growing leading edge separation bubbles' size are different. Case 3 has bigger leading edge separation bubble and it develops to the downstream widely. The lift coefficient is local minimum when leading edge separation bubbles burst at the suction side of the airfoil in case 3 but in case 1, leading edge separation bubble is reattached at the upper side of

the AMD and force fluctuation is relatively small. So force fluctuations of case 3 are relatively big because of growing, developing leading edge separation bubble and bursting of it.

3.4 Mean velocity and pressure profiles near the leading edge of the no controlled and the controlled airfoils

Figure 3.9 shows the velocity profiles near the leading edge of the controlled case 1 and the no controlled airfoil. These profiles are extracted at five points on the airfoil surface. Black and red lines indicates the velocity profiles of the no controlled and controlled case, respectively. As shown in this figure, the controlled airfoil case 1 has larger velocity at the edge of the boundary layer and reversed flow in the recirculation bubble near the leading edge.

Figure 3.10 shows the velocity and pressure profiles near the leading of the controlled case 1 and the no controlled airfoil. These profiles are extracted at the three points at the suction side of the airfoils. Solid and dashed lines indicate velocity and pressure profiles, respectively and black and blue lines indicates the no controlled and controlled case, respectively. By increasing of the velocity of the boundary layer edge and recirculation flow, the velocity gradient of the case 1 is bigger than that of the no controlled case. It implies that the mean separation bubble strength is increased and the pressure is reduced.

3.5 Mean streamlines of the no controlled and the controlled airfoils

Figure 3.11 shows the mean streamlines. The controlled cases have the smaller separation bubble than the no controlled case. The

AMD prevents flow separation from proliferating further and reattachment occurs at the upper side of the AMD. Due to the flow reattachment at the upper side of the AMD, flow separation occurs at the further downstream of the trailing edge and this contributes to the drag reduction.

3.6 Comparison of the Mean surface coefficients for each cases

Fig 3.12 shows the mean surface pressure coefficients of the no controlled case and controlled cases. Drawing surface pressure coefficients along the surface of the controlled airfoil like the left-upper figure explains the lift enhancement well. At the flow being accelerated by the stagnation point, there exist suction peak. Before the root of the AMD there exists a low pressure region and this is caused by increasing of the amplitude of the leading edge separation bubble strength. Flow reattachments at the upper side of the AMD occur and pressures are recovered.

3.7 Instantaneous 3 dimensional vortical structures

Figure 3.13 shows the instantaneous vortical structures around the airfoil with AMD using λ_2 -structures which are proposed by Jeong and Hussain for the no controlled case and the controlled case 2. The amplitude of λ_2 is -1000 and pressure is colored at the λ_2 structures. Thorough λ_2 structures, complex vortical structures are developed from the leading edge and reattachments are observed in the trailing edge of AMDs.

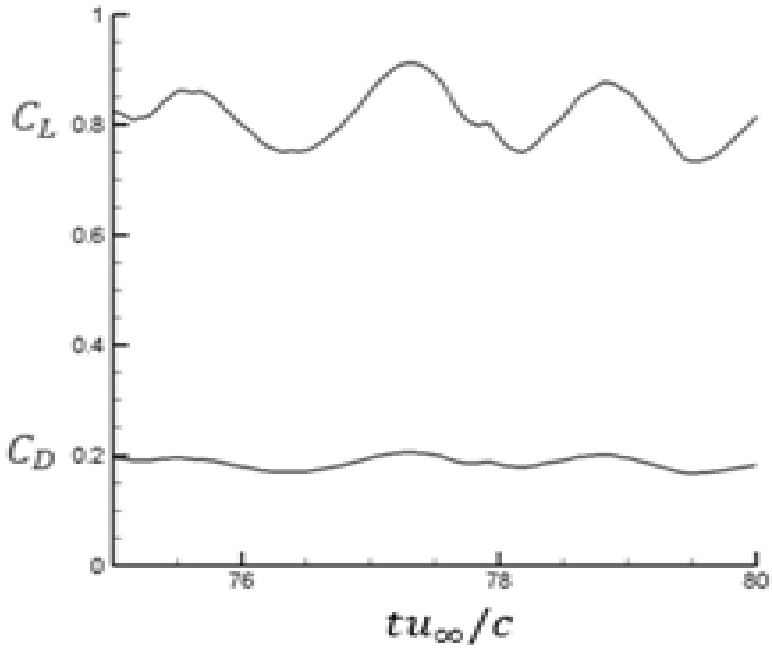

FIGURE 3.1 The time traces of the drag (red solid line) and lift (blue solid line) coefficients of the no controlled SD7003 airfoil.

	C_L	C_D
Catalano *et al.*, 2010 ,LES	0.7	0.25
Catalano *et al.*, 2010, RANS	0.9	0.08
Ol *et al.*, 2005, Exp	1.05	-
Galbraith *et al.*, 2008, ILES	0.95	0.4
Galbraith *et al.*, 2008, XFOIL N=9	0.8	0.6
Selig *et al.*, 1996, Exp	0.9	-
Kim (SNU wind tunnel), Exp	0.9	0.2
Present	0.82	0.19

Table 3.1 The previous results of the numerical simulation for the SD7003 airfoil at the angle of attack, 12 degree.

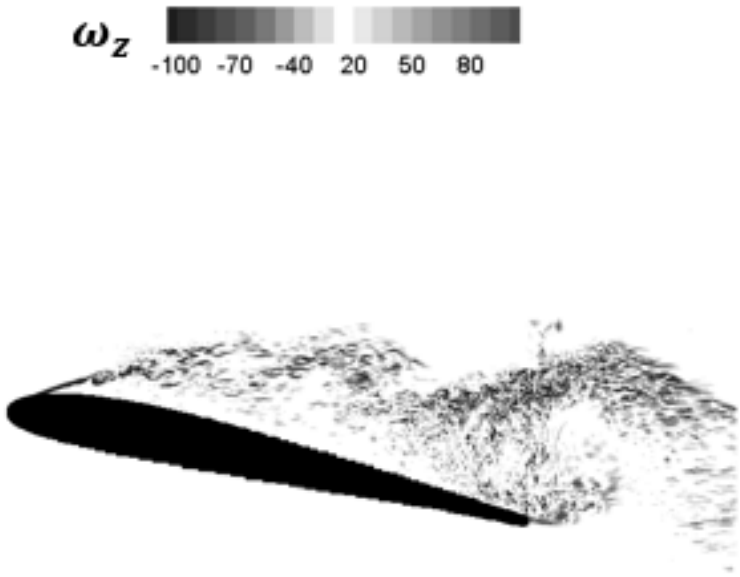

FIGURE 3.2 The instantaneous spanwise vorticity contour around the SD7003 airfoil.

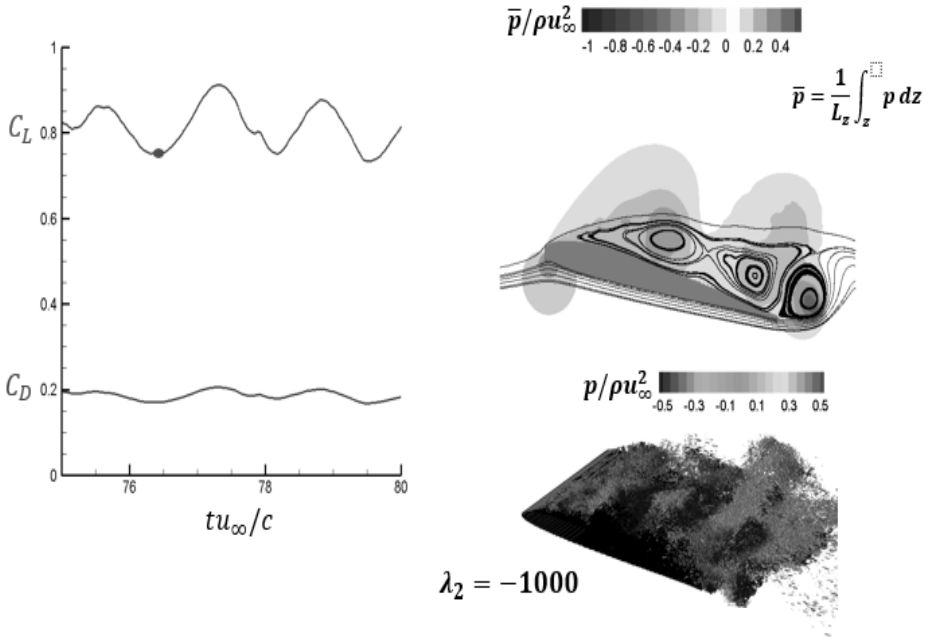

FIGURE 3.3 Spanwise averaged pressure contour and three dimensional vortical structure around the SD7003 airfoil with the lift coefficient being local minimum.

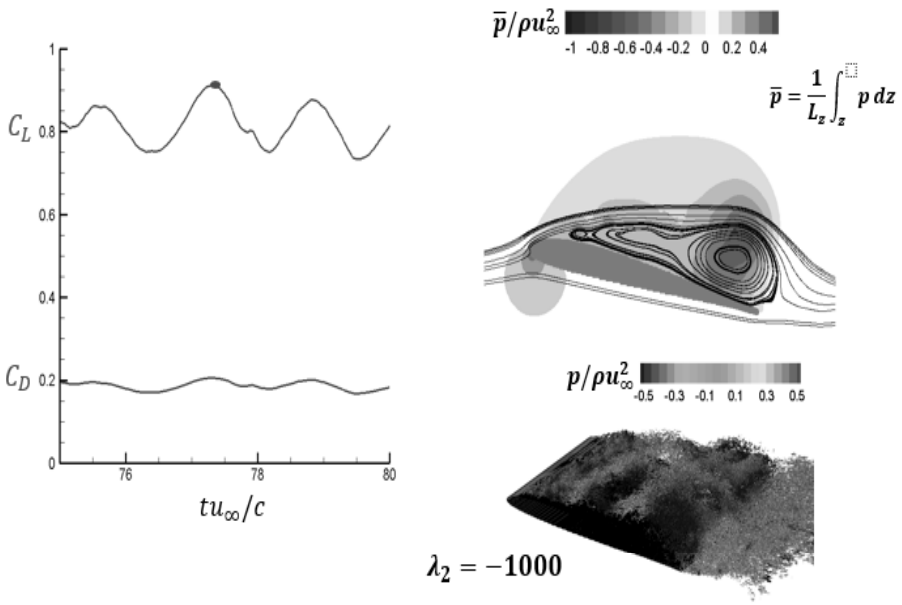

FIGURE 3.4 Spanwise averaged pressure contour and three dimensional vortical structure around the SD7003 airfoil as the lift coefficient is local maximum.

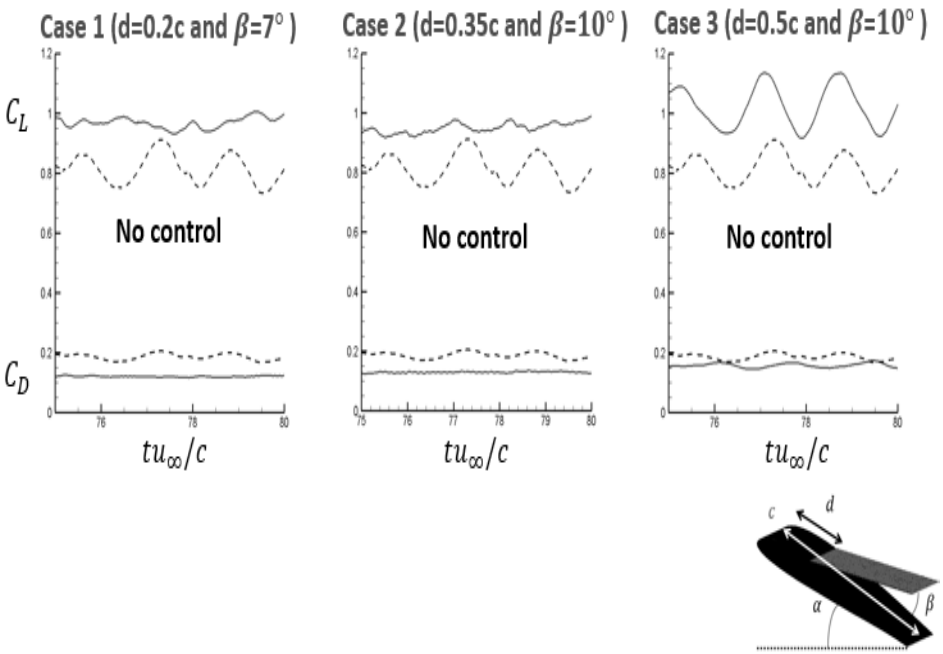

FIGURE 3.5 The time traces of the drag and lift coefficients of the controlled airfoils (solid red lines) comparing with those of the no controlled airfoil (dashed black lines).

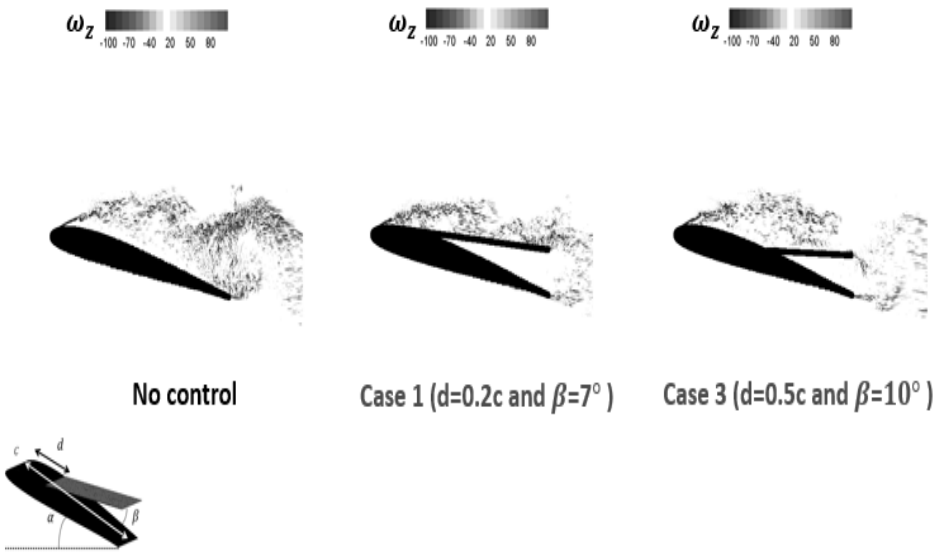

FIGURE 3.6 The instantaneous spanwise vorticity contours of the no controlled airfoil (left), the controlled case 1(middle) and the controlled case 3 (right).

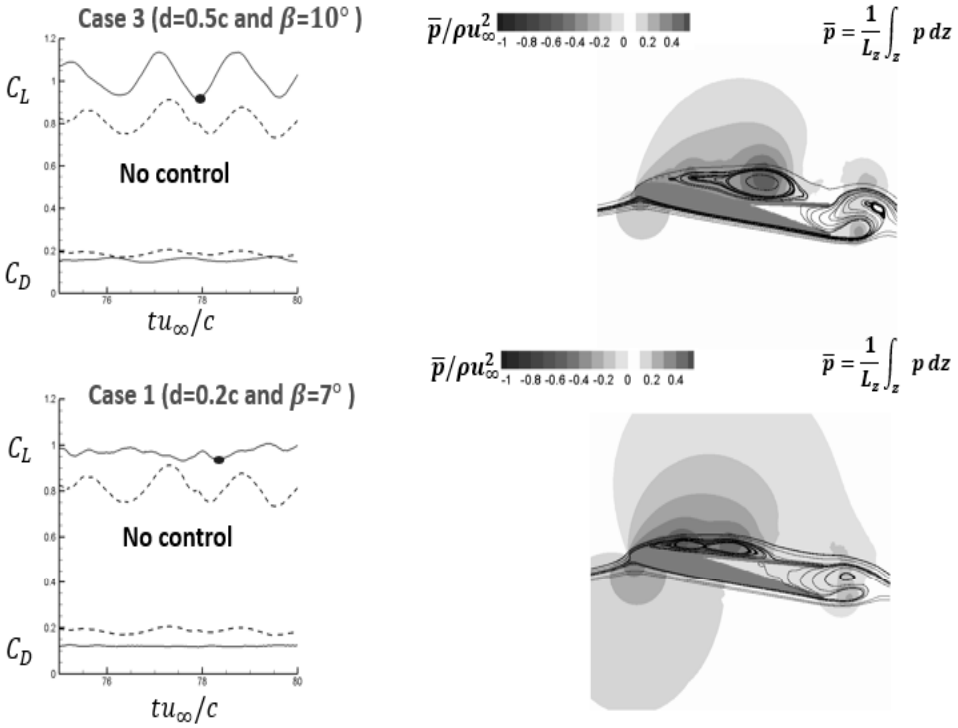

FIGURE 3.7 The time traces of the lift and drag coefficients and spanwise averaged pressure contours of the no controlled case (dashed lines) and the controlled cases (red solid lines).

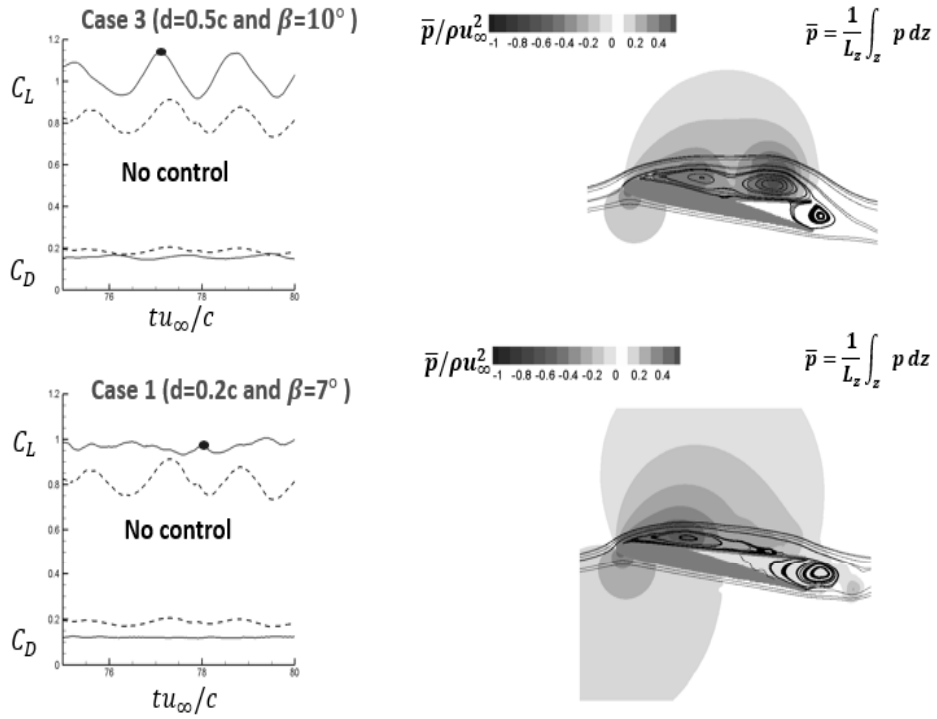

FIGURE 3.8 The time traces of the lift and drag coefficients and spanwise averaged pressure contours of the no controlled case (dashed line) and the controlled cases (solid red lines).

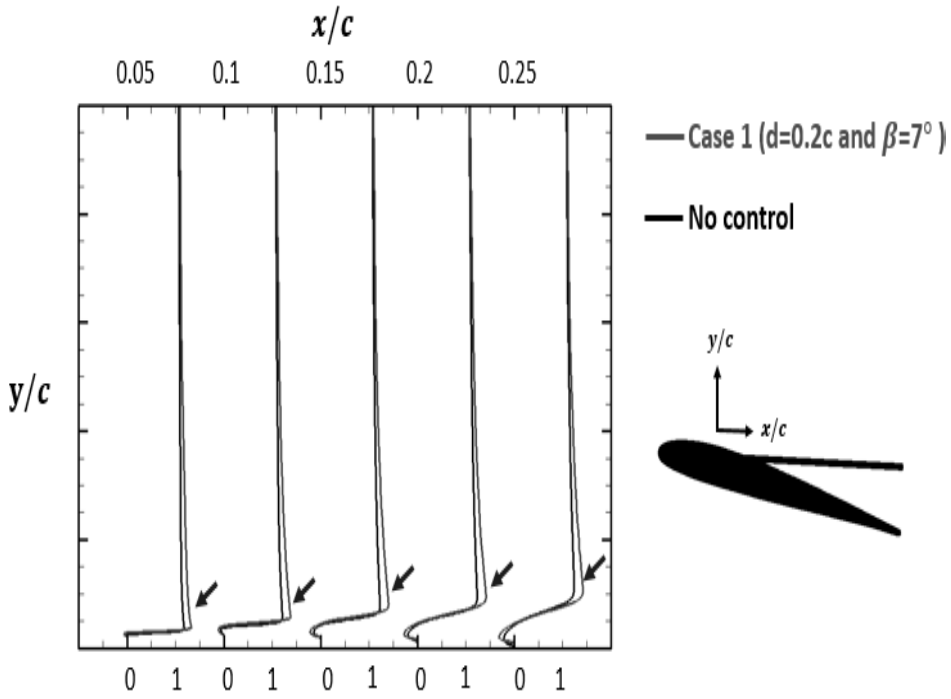

FIGURE 3.9 The velocity profiles near the leading edge of the controlled case 1 (red solid lines) and the no controlled airfoil (black solid lines).

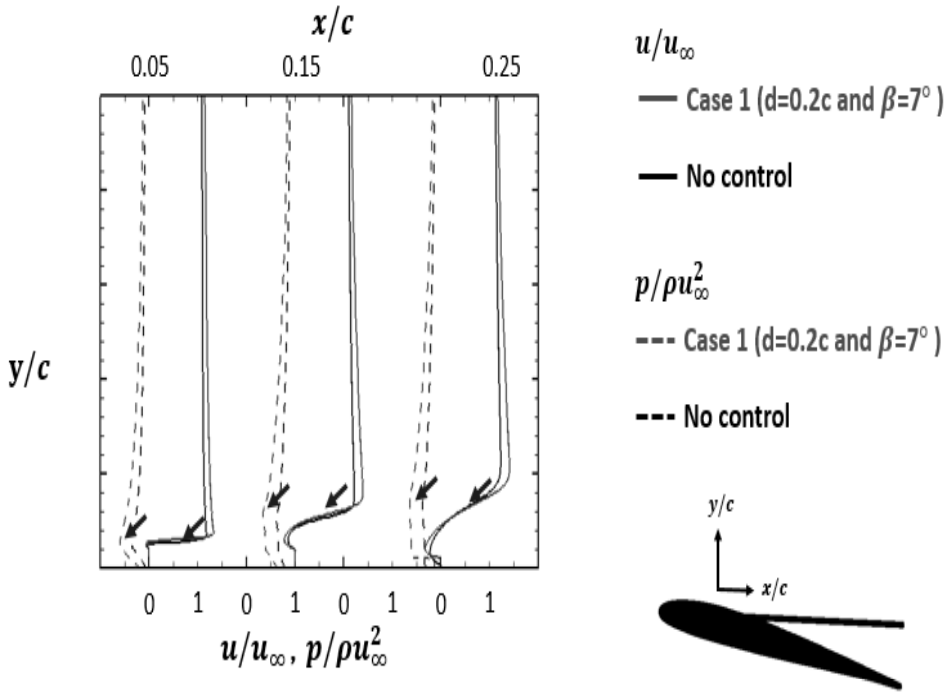

FIGURE 3.10 The velocity and pressure profiles near the leading of the controlled case 1 and the no controlled airfoil. Solid and dashed lines indicate velocity and pressure profiles, respectively and black and blue lines indicates the no controlled and controlled cases, respectively.

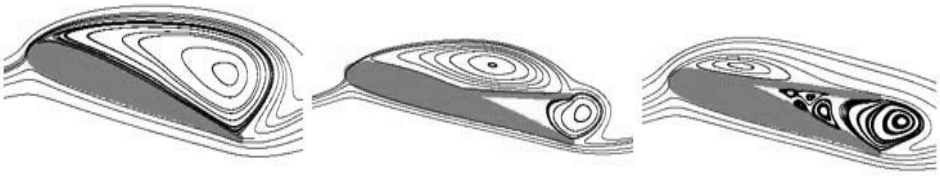

No control　　Case 3 (d=0.5c and β=10°)　　Case 1 (d=0.2c and β=7°)

FIGURE 3.11 The mean streamlines of the each cases.

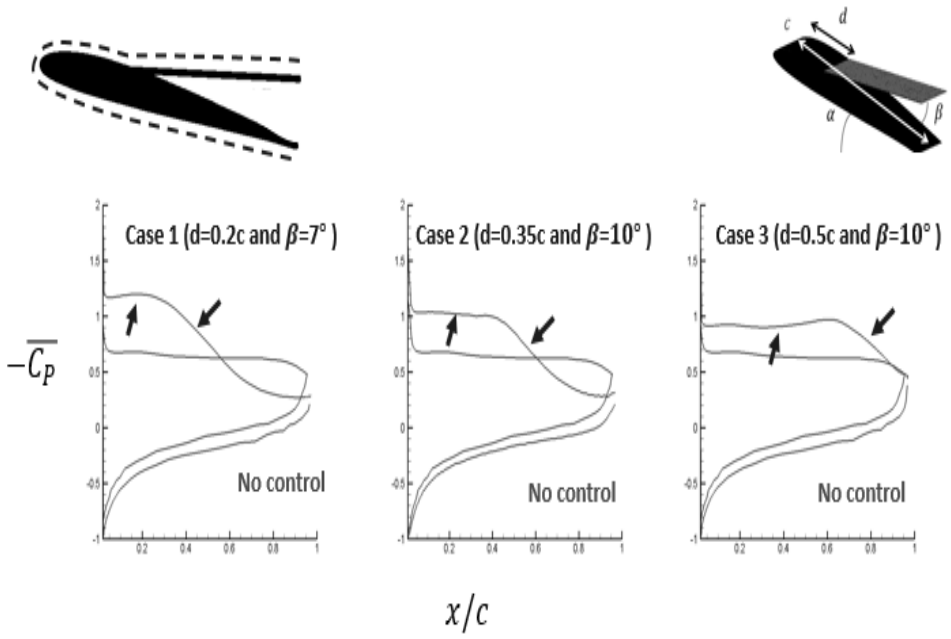

Figure 3.12 The mean surface pressure coefficients of the no controlled case (red solid lines) and the each controlled cases (blue solid lines).

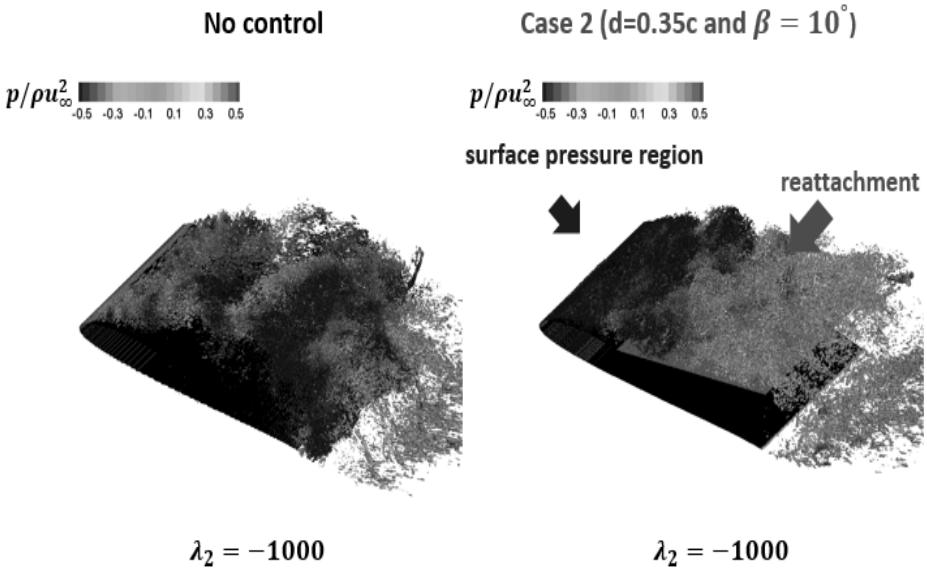

Figure 3.13 The instantaneous vortical structures around the airfoil with AMD using λ_2 −structures which are proposed by Jeong and Hussain for the no controlled case and the controlled case 2.

Chapter 4

Summary and Conclusion

In the present study, the flows around the SD7003 airfoil with and without AMD were investigated using a large eddy simulation at the post-stall angle of attack, 12°.

The aerodynamic coefficients (lift and drag coefficient) of the controlled airfoils were compared with those of the no control airfoil and the controlled airfoils had the better performances than the no controlled airfoil.

The low surface pressure region existed in front of the AMD because of the increased strength of the separation bubble.

The AMD prevented the leading edge separation bubble from proliferating further on the suction side of the airfoil and as a result flow reattachment occurred at the upper side of the AMD.

Bibliography

Bechert, D., Bruse, M., Hage, W. and Meyer, R. 1997 Biological surfaces and their technological application—laboratory and flight experiments on drag reduction and separation control. AIAA paper, **1**, No. 1960, pp. 22−30.

Catalano, P. and Tognaccini, R. 2010 Turbulence modeling for low−Reynolds−number flows. *AIAA J.* **48**(8), 1673−1685

Choi, H., Park, H., Sagong, W. and Lee, S. 2012 Biomimetic flow control based on morphological features of living creatures. Phys. Fluids, **24**, 121302.

Galbraith, M. C. and Visbal, M. R. 2008 AIAA Implicit large eddy simulation of low Reynolds number flow past the sd7003 airfoil. AIAA aerospace and sciences meeting and exhibit, Jan., 7−10, Reno, Nevada.

Hucho, W. H. and Sovran G. 1993 Aerodynamics of road vehicles, Annual Review of Fluid Mechanics. **25**, 485–537

Jeong, J. and Hussain, F., 1995, On the identification of a vortex, J. Fluid Mech., **285**, pp. 69−94.

Kernstine, K., Moore, C., Cutler, A. and Mittal, R. 2008 Initial characterization of self−activated movable flaps, "pop−up feathers" . AIAA aerospace and sciences meeting and exhibit, Jan., 7−10, Reno, Nevada.

Kim, D., Lee, H. and Choi, H. 2014 Drag reduction of a three−dimensional model vehicle using automatic moving deflector. KSME autumn conference, Nov., 11−14, 2014, Kwangju, Korea.

Kim, J., Kim, D. and Choi, H. 2001 An immersed boundary finite volume method for simulations of flow in complex geometries. J. Comput. Phys., **171**, pp. 132−150.

Kim, K., Baek, S. and Sung, H. 2002 An implicit velocity decoupling procedure for the incompressible Navier-Stokes equations. Int. J. Numer. Methods Fluids, **38**, pp. 125-138.

Lee, J., Choi, H. and Park, N. 2010 Dynamic global model for large eddy simulation of transient flow. Phys. Fluids, **22**, 075196.

Liebe, W. 1979 Der Auftrieb am Tragugel: Entstehung und Zusammenbruch, Aerokurier. **12**, 1520-1523

Meyer, R., Hage., W. and Bechert, D. 2007 Separation control by self-activated movable flaps. AIAA paper, **45**, No.1, pp. 191-199.

Ol, M. V., Hanff, E., Mcauliffe, B., Scholz, U. and Kahler, C. 2005 Comparison of laminar separation bubble measurements on a low Reynolds number airfoil in three facilities. *AIAA* paper 2005-5149

Schatz, M., Knacke, T., Thiele, F., Meyer, R., Hage, W. and Bechert, D.W. 2004 Separation control by selfactivated movable flaps. AIAA Paper 1243

Schlűter, J. 2010 Lift enhancement at low Reynolds numbers using self-activated movable flaps. J. Aircraft, **47**, No.1, pp. 348-351.

Selig, M. S., Guglielmo, J. J., Broeren, A. P. and Giguere, P. 1995 Summary of low speed airfoil Data, **1**, Soartech Aero, Virginia Beach, VA

Wang, C. H. and Schlüter, J. 2012 Stall control with feathers: Self-activated flaps on finite wings at low Reynolds numbers. Comptes Rendus Mécanique, **340**, 57-66

레이놀즈수 60,000에서 Automatic moving deflector를 이용한 SD7003 익형의 실속 제어

서울대학교 대학원
기계항공공학부
천소민

요 약

본 연구에서는 새의 깃털을 모방한 자동 디플렉터를 SD7003 익형의 흡입면에 부착하여 레이놀즈수 60,000에서 그에 따른 공력 성능 및 주위 유동현상을 큰 에디 모사 기법을 이용하여 예측하였다. 자동 디플렉터가 뜨는 조건인 실속 이후의 받음각 12도에서 계산이 수행되었으며 결과로 도출된 양력, 항력계수들이 기존 값들과 잘 일치하는 것을 확인하였다. 자동 디플렉터의 부착으로 인해 각각의 제어사례 1 - 3에 대하여 양력계수가 최대 10% 정도 증가하였고 항력은 최대 30%까지 감소하는 것을 확인하였으며 힘 섭동량 또한 크게 감소하였다. 자동 디플렉터 부착으로 인하여 익형의 흡입면에 유동박리가 크게 감소하고 흡입면에 낮은 압력구간이 존재하여 양력이 증가하였으며 유동박리 또한 익형의 끝단에서부터 더 후류에 생성되어 항력 또한 감소하였다.

주요어: 큰 에디 모사, SD7003 익형, 자동 디플렉터

학번: 2012-23945